EES Solar

PAPER

View Article Online
View Journal

Cite this: DOI: 10.1039/d5el00193e

Tailoring crystallization dynamics and phase evolution of co-evaporated pure α-$FAPbI_3$ for enhanced device performance

Francesca Zarotti, †‡*[a] Erica Magliano, †[b] Suresh Podapangi, [a] Federico Trezzini,[a] Elham Ghavidel, [a] Venanzio Raglione, [b] Marco Di Giovannantonio, [b] Francesco Di Giacomo, §[a] Alessandro Coati, [c] Roberto Felici [b] and Aldo Di Carlo *[ab]

Formamidinium lead iodide ($FAPbI_3$) is among the most promising perovskite compositions for high-efficiency photovoltaics. However, its thermal co-evaporation remains technically challenging due to inherent phase instability and thermal decomposition of the organic precursors. In this work, we demonstrate an additive-free thermal co-evaporation of pure $FAPbI_3$, by sequentially employing multiple sources of formamidinium iodide (FAI). This strategy effectively mitigates process instabilities of FAI during prolonged evaporation, enabling the growth of thick perovskite films with improved morphology. Furthermore, we show that the introduction of an intermediate annealing step significantly enhances crystallization dynamics during thickness scaling, resulting in highly ordered and coherent film structures. A systematic investigation of substrate temperature during deposition highlights its crucial role in phase purity and crystallinity. Notably, films grown at 60 °C exhibit superior structural order and effective suppression of the undesired hexagonal non-perovskite phases, as confirmed by X-ray diffraction analysis. We also compare two widely used hole transport layers, MeO-2PACz and PTAA, and show that, although MeO-2PACz promotes α-phase formation, it poses challenges related to film morphology and processing reproducibility. Finally, devices employing PTAA in a p–i–n architecture achieve a power conversion efficiency of 18.5% using pure, thermally evaporated $FAPbI_3$.

Received 19th November 2025
Accepted 15th May 2026

DOI: 10.1039/d5el00193e

rsc.li/EESSolar

Broader context

Formamidinium lead iodide ($FAPbI_3$) continues to attract significant interest as a highly promising perovskite absorber for next-generation photovoltaics, yet its full potential remains constrained by challenges in vacuum-based fabrication. Thermal co-evaporation, a technique well suited for industrial scaling, has been particularly difficult for $FAPbI_3$ due to phase instability and decomposition of organic iodide precursors. As the field increasingly moves toward solvent-free and highly controlled deposition methods, developing reliable approaches to evaporate $FAPbI_3$ is both timely and essential. This work addresses these limitations by introducing an additive-free co-evaporation strategy that employs multiple FAI sources, mitigating thermal degradation and enabling the growth of high-quality, thick films. The study further elucidates the critical influence of substrate temperature and intermediate annealing on phase purity and crystallization, offering insights into controlling α-phase formation. By comparing MeO-2PACz and PTAA hole transport layers and demonstrating efficient p–i–n devices, the results advance the technological feasibility of vacuum-processed $FAPbI_3$ photovoltaics. By identifying processing windows that yield thick, uniform, and highly crystalline α-phase films, this work contributes to establishing vapor-phase deposition as a robust and industrially viable route for perovskite photovoltaics.

1. Introduction

Perovskite solar cells (PSCs) have emerged as a highly promising photovoltaic technology due to their optoelectronic properties, improved light absorption, direct and tunable bandgap, and high carrier mobility.[1,2]

Among the various perovskite compositions, formamidinium lead triiodide ($FAPbI_3$, or FAPI, chemical formula: $CH(NH_2)_2PbI_3$) stands out thanks to its optimal bandgap of approximately 1.48 eV, which closely matches the optimal value predicted by the Shockley–Queisser limit for the maximum solar energy conversion efficiency.[3] $FAPbI_3$ also exhibits

[a]C.H.O.S.E. (Center for Hybrid and Organic Solar Energy), Electronic Engineering Department, University of Rome Tor Vergata, Via del Politecnico 1, Rome, 00118, Italy. E-mail: francesca.zarotti@uniroma2.it

[b]CNR – Istituto di Struttura della Materia (CNR-ISM), via Fosso del Cavaliere 100, 00133 Roma, Italy

[c]Synchrotron SOLEIL, L'Orme des Merisiers, Saint-Aubin, 91192 Gif sur Yvette, France

† Both authors contributed equally to this work.

‡ Present address: ENEA, Italian National Agency for New Technologies, Energy and Sustainable Economic Development, Via Enrico Fermi, 45, 00044 Frascati, Rome, Italy.

§ Present address: SunXT S.r.l., Via Eusebio Chini 15, 00147, Rome, Italy.

enhanced thermal stability compared to other widely investigated hybrid metal halide perovskites (MHPs), such as $MAPbI_3$, attributed to the formamidinium proton being relatively inert and making it a more suitable candidate for long-term operational stability at elevated temperatures.[4,5]

Moreover, the compositional simplicity of $FAPbI_3$, consisting of a single A-site cation and a single halide, represents a significant advantage compared to alloyed perovskites incorporating multiple A-site cations (*e.g.*, Cs^+ and MA^+) or mixed halides (I^-/Br^-). Although compositional engineering through cation or halide mixing has been widely employed to enhance structural stability, it increases the chemical complexity and the bandgap.[6] Additionally, halide compositions are well known to be prone to halide segregation under thermal or light stress.[7,8]

Achieving and retaining the photoactive α-phase of $FAPbI_3$ during crystallization and under operational conditions remains a critical challenge. In fact, while the black photoactive α-phase (cubic) exhibits excellent optoelectronic properties, it is thermodynamically metastable at room temperature and readily converts into the wide-bandgap (~2.4 eV) yellow δ-phase (hexagonal) during crystallization and under prolonged exposure to ambient conditions. This transformation is further accelerated in the presence of moisture and at elevated temperatures.[9–12] This phase transition undermines device efficiency and durability. Numerous stabilization approaches, such as cation/halide mixing or additive engineering, have been proposed.[13–22] However, these solutions often come at the cost of increased complexity and cause bandgap widening, defect formation, or inhomogeneous film morphology, ultimately limiting their practical scalability.

Remarkable performance of pure α-$FAPbI_3$-based solar cells has been enabled by a series of innovative approaches aimed at improving phase stability and optoelectronic quality.[23,24] For instance, Huang *et al.* employed hexafluorobenzene (HFB) to lower the chemical potential of formamidinium iodide (FAI), effectively slowing down its reaction with lead iodide (PbI_2). This strategy helped suppress the formation of the undesired δ-phase, which would otherwise compromise device stability.[23] In a separate study, Cao *et al.* showed that the incorporation of a triphenylamine (TPA)-functionalized ligand significantly enhances charge transport in $FAPbI_3$ perovskite solar cells. This molecular engineering led to improved film quality and boosted the efficiency of 2D/3D $FAPbI_3$-based devices, with a champion power conversion efficiency (PCE) of 25.7%.[24] These high performances were all achieved using solution-based deposition techniques, which remain the leading fabrication methods for PSCs. This is largely attributed to the low cost and accessibility of solution processing, which have enabled rapid development of efficient synthesis and passivation protocols.[25,26] As a result, solution-processed perovskites, including all various formulations, and pure $FAPbI_3$, continue to lead the field of PSC development.

In contrast, thermal evaporation has received comparatively less attention and lags behind in efficiency.[25] The current record for vacuum-deposited PSCs is 20.6% for a co-evaporated $MAPbI_3$-based device.[27] While vapor deposition offers significant advantages in terms of scalability, reproducibility, and compatibility with industrial processes,[28] its development has been hindered by challenges related to the thermal evaporation of organic salts due to their high-vapor pressure and volatile behavior.[29–32] Specifically, FAI presents a major challenge due to its thermal instability and decomposition.[32,33] As shown by Kroll *et al.*, FAI tends to degrade at elevated source temperatures, forming unwanted byproducts that increase the background pressure inside the chamber.[32] This degradation not only reduces the amount of FAI that successfully reaches the substrate, but also leads to a stoichiometric imbalance in the resulting perovskite film. Moreover, the development of thermally evaporated $FAPbI_3$ has been further constrained by the absence of well-defined additive engineering protocols compatible with vacuum deposition processes, making it more challenging to replicate the strategies adopted in solution-based systems.

In this work, we demonstrate the additive-free thermal co-evaporation of pure $FAPbI_3$ by sequentially employing multiple FAI sources, rather than operating them in parallel. Our strategy effectively circumvents the time-dependent evolution of the FAI source during prolonged evaporation and enables the growth of thick FAPI layers overcoming difficulties in FAI control. Furthermore, we demonstrate that introducing an intermediate annealing step improves the crystallization dynamics when increasing the perovskite thickness, leading to a more coherent and better-ordered film structure. We further investigate the impact of substrate temperature and substrate nature on perovskite film formation and properties.

The role of substrate temperature during co-evaporation has been extensively studied for $MAPbI_3$, where the substrate temperature strongly influences MAI adsorption and thus final film morphology and stoichiometry.[31,34–37] However, the influence of temperature on FAI-based compositions has received limited attention. Gil-Escrig *et al.* conducted a systematic study on $Cs_{0.2}FA_{0.8}Pb(I_{0.8}Br_{0.2})_3$ showing that reduced FAI incorporation at elevated temperatures can promote improved film morphology.[38] Building on this, we explore co-evaporated FAPI growth at four different substrate temperatures (T_{sub}): −10 °C, 20 °C, 50 °C, and 60 °C. Structural and morphological characterization reveals a clear evolution in crystallinity and phase purity. Notably, GIXD analysis on films grown at 20 °C and 60 °C highlights that 60 °C promotes a higher degree of crystalline order and effectively suppresses the formation of undesired hexagonal phases.

As for the substrate nature, recent studies have highlighted the significant role of the hole transport layer (HTL) in influencing perovskite film growth during thermal evaporation.[39–43] In particular, unwashed [*n*]-phosphonic acid carbazole (*n*PACz) layers promote FAI adsorption through exposed phosphonic acid groups, which interact strongly with iodide *via* hydrogen bonding.[39] This interaction creates an energetic barrier that suppresses the transformation of the photoactive α-$FAPbI_3$ phase into the undesirable δ-phase, thereby kinetically stabilizing the desired perovskite structure. The improved FAI adhesion on *n*PACz surfaces allows for a lower FAI deposition rate to achieve optimal stoichiometry and crystallinity, promoting the formation of high-quality perovskite films.

Conversely, these same interactions between phosphonic acid and hydrogen groups can become problematic for bromide-containing compositions, as highlighted by Öz *et al.*[42] Castro-Méndez *et al.* further demonstrated that the migration of excess phosphonic acid species during film growth contributes positively to α-phase stabilization by maintaining a steady supply of adsorbed organic precursors at the growth front, thereby reducing the energy barrier for crystallization and enhancing the FAI adsorption rate.[40] Nevertheless, excess *n*PACz molecules can negatively impact device performance by forming an insulating interfacial layer or inducing FAI excess, which may reduce open-circuit voltage (V_{OC}) and short-circuit current density (J_{SC}).[39,41] To mitigate this, a mild rinsing step is sometimes employed, though it risks partial exposure of the underlying ITO and uncontrolled interfacial effects.

To clarify the influence of the underlying substrate on the crystallization behavior of co-evaporated $FAPbI_3$, we conducted a comparative study using [2-(3,6-dimethoxy-9*H*-carbazol-9-yl) ethyl]phosphonic acid (MeO-2PACz) and poly[bis(4-phenyl)(2,4,6-trimethylphenyl)amine] (PTAA) as HTLs. The results showed that MeO-2PACz more effectively promotes the formation of the photoactive α-$FAPbI_3$ phase and suppresses non-perovskite phases compared to PTAA. However, this advantage is counterbalanced by inferior film morphology and limited process reproducibility. Consequently, PTAA yielded superior device performance under the same growth conditions. By fine-tuning critical parameters – including the deposition procedure, substrate temperature, and the HTL – we achieved enhanced performance in a p–i–n architecture, reaching a power conversion efficiency of 18.5% with thermally evaporated pure $FAPbI_3$. An impressive long-term stability is demonstrated in shelf life, and the final encapsulated device shows a T_{80} (time in which the PCE reaches 80% of the initial PCE)[44] of 400 hours.

2. Results and discussion

We investigate the optimal process conditions and the effect of the substrate on the growth quality of $FAPbI_3$ deposited by the co-evaporation of FAI and PbI_2.

The precursor quantities were measured and loaded into each crucible prior to every deposition run. To prevent FAI decomposition during evaporation, the source temperature was maintained at 210 °C. Higher temperatures were deliberately avoided to minimize the risk of carbonization or thermal degradation of FAI during the deposition process, as discussed in the SI.[32,33] Co-deposition started once the crucibles reached their target temperatures: 345 °C for PbI_2 and 210 °C for FAI (further details can be found in the Experimental section). The substrate temperature was regulated using a stainless steel holder cooled using a water–glycol mixture connected to an external temperature bath. Perovskite films were deposited at substrate temperatures ranging from −10 °C to 60 °C.

Owing to the large impact of temperature on crystallization and morphology of co-evaporated $FAPbI_3$, we first explored the impact of substrate temperatures on deposition. A preliminary study was conducted by testing a range of possible substrate temperatures (−10 °C, 20 °C, 50 °C, and 60 °C) during a continuous co-deposition process of 120 min. XRD analysis (Fig. S2) revealed enhanced crystallinity at 60 °C, as indicated by the lowest full width at half maximum (FWHM) and highest intensity of the α-phase (100) peak, which is evidence of a more ordered and crystalline structure. Notably, good crystallinity was also observed at 20 °C. Based on these results, 20 °C and 60 °C were selected for further investigation using grazing-incidence X-ray diffraction (GIXD).

Studies of the structural properties of $FAPbI_3$ perovskite were conducted on different films deposited on two different HTLs: MeO-2PACz, hereafter referred to as the self-assembled monolayer (SAM), and PTAA. The abovementioned substrate temperatures of 20 °C and 60 °C were employed for both the HTLs under examination.

Multiple FAI sources were employed at different stages of the deposition to modulate the incorporation dynamics, effectively preventing time-dependent changes in the FAI source under prolonged evaporation.

Films were deposited for varying durations (20, 100, 200, and 300 minutes) hereafter referred to as Type-20, Type-100, Type-200, and Type-300, respectively. In Type-200, two FAI sources were employed consequently for 100 minutes each, without breaking the vacuum.

Additionally, samples labelled with Type-300A underwent a two-step deposition process: an initial 200-minute deposition (Type-200) followed by annealing (150 °C for 15 min) and then an additional 100-minute deposition. A final annealing step at 150 °C for 15 min was always performed in order to promote the transition from the δ-phase to the α-phase (Fig. S3 and S4). A schematic of the different deposition processes is shown in Fig. 1.

We initially tested perovskite fabrication using a continuous 200-minute $FAPbI_3$ evaporation process, without any FAI substitution or modification during vacuum deposition (Fig. 2). This study was performed on glass/ITO/PTAA with a substrate temperature of 60 °C during co-evaporation. The sample prepared *via* continuous 200-minute $FAPbI_3$ evaporation (indicated as "Continuous-200") exhibits a more pronounced PbI_2 peak, indicative of incomplete conversion, as compared to the spectrum of the Type-200 perovskite film. In contrast, the Type-200 sample displays a sharp and intense (100) perovskite peak along with a weaker PbI_2 signal, indicating more complete and uniform perovskite formation, as also verified by XRD analysis in ambient air over time (Fig. S5). Notably, both the Type-200 and the Continuous-200 deposition processes yield perovskite films with similar thicknesses (∼280 nm, Fig. 2), suggesting that the formed PbI_2 does not result from under conversion due to insufficient FAI precursor supply but rather from a different evaporation behavior of FAI.

To further investigate its behavior during prolonged evaporation, we performed ^{1}H-NMR measurements on FAI powder collected at different evaporation times (Fig. S6). From the comparison of the ^{1}H-NMR spectra, the evaporation process appears to promote a progressive purification of FAI, as evidenced by the systematic increase in the $-NH_2$ peak intensity when extending the evaporation time from 20 to 200 minutes.

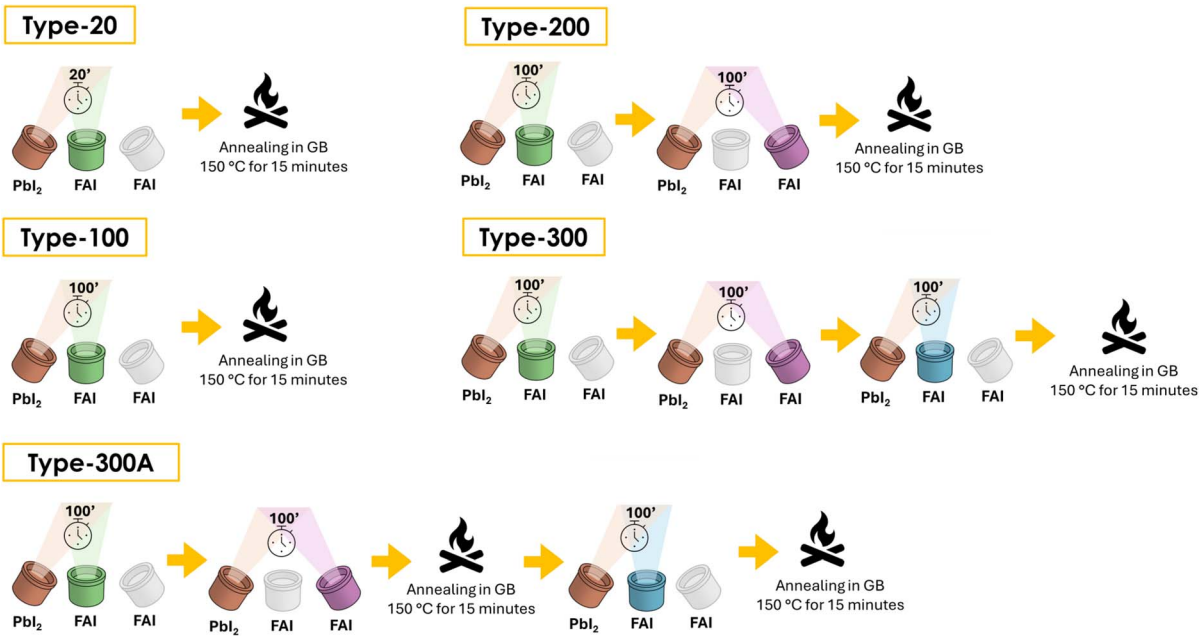

Fig. 1 Schematics of different deposition processes of $FAPbI_3$, labelled as Type-20, Type-100, Type-200, Type-300, and Type-300A.

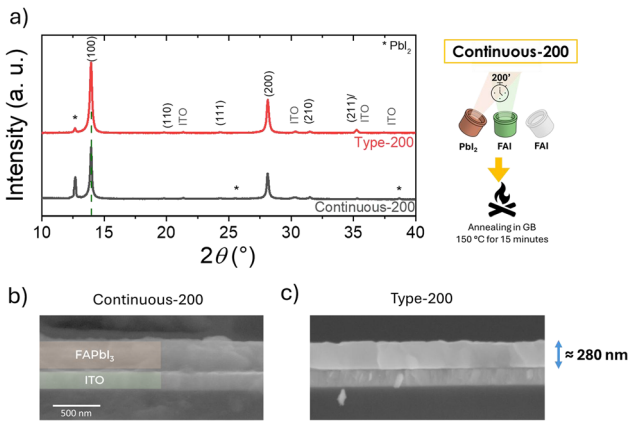

Fig. 2 (a) XRD spectra of FAPI deposited continuously for 200 min (Continuous-200) and Type-200 FAPI, on glass/ITO/PTAA with substrate temperature set at 60 °C during the co-evaporation process. A schematic of the Continuous-200 process is also shown on the right. (b and c) Cross-section SEM images of the two perovskite types.

However, the sample evaporated for 20 minutes exhibits a lower signal intensity compared to pristine FAI. This behavior may be attributed to the initial formation of byproducts (*e.g.*, HI), which could induce peak broadening and consequently reduce the apparent signal intensity. Upon increasing the evaporation time, these byproducts are progressively removed, in agreement with literature reports,[32] resulting in a gradual sharpening and intensification of the $-NH_2$ peak.[33] We hypothesize that prolonged evaporation of FAI may lead to progressive physical and chemical changes in the precursor residue within the crucible, driven by the depletion of volatile species and alterations in the surface morphology of the FAI powder. These changes can, in turn, affect the stoichiometry and dynamics of the vapor phase.

To circumvent FAI instability over prolonged evaporation time, each FAI source was employed for a maximum of 100 minutes. Therefore, for longer deposition processes (*i.e.*, Type-200, Type-300, and Type-300A), FAI was introduced from different sources sequentially, rather than simultaneously, to further control the film composition and morphology.

The samples under investigation are indicated as "HTL_substrate temperature", *e.g.* PTAA_20 indicates the $FAPbI_3$ grown on PTAA with a substrate temperature of 20 °C during vacuum deposition. For each sample, a comprehensive peak and phase identification analysis was performed starting from the spectra reported in Fig. 3. The spectra were measured and normalized to the substrate reference peak to ensure consistent comparison.

Structurally, both the α-phase (cubic) and δ-phase (hexagonal) are present in the samples, except for SAM_60 where only the α-phase is detected (Fig. 3). In particular, the two most intense peaks are located at $q \approx 0.99$ Å^{-1} [(100)] and $q \approx 1.98$ Å^{-1} [(200)] for the α-phase and at $q \approx 0.84$ Å^{-1} [(100)] and $q \approx 1.85$ Å^{-1} [(201)] for the δ-phase, with the single polytype 2H detected (Fig. S7).

In the case of PTAA-based samples (Fig. 3a and b), increasing the substrate temperature to 60 °C enhances the formation of the photoactive α-cubic phase of $FAPbI_3$ while reducing the presence of hexagonal δ-phase impurities, compared to films deposited at 20 °C. A similar trend is observed for samples deposited on the SAM (Fig. 3c and d), where the promotion of the α-phase is even more pronounced. In particular, no δ-phase is detected at 60 °C on the SAM (Fig. 3d), whereas at 20 °C (Fig. 3c), a weak δ-phase peak begins to emerge from the Type-100 deposition condition onward.

Notably, the α-phase is present in all samples after only 20 minutes of deposition, regardless of substrate type or

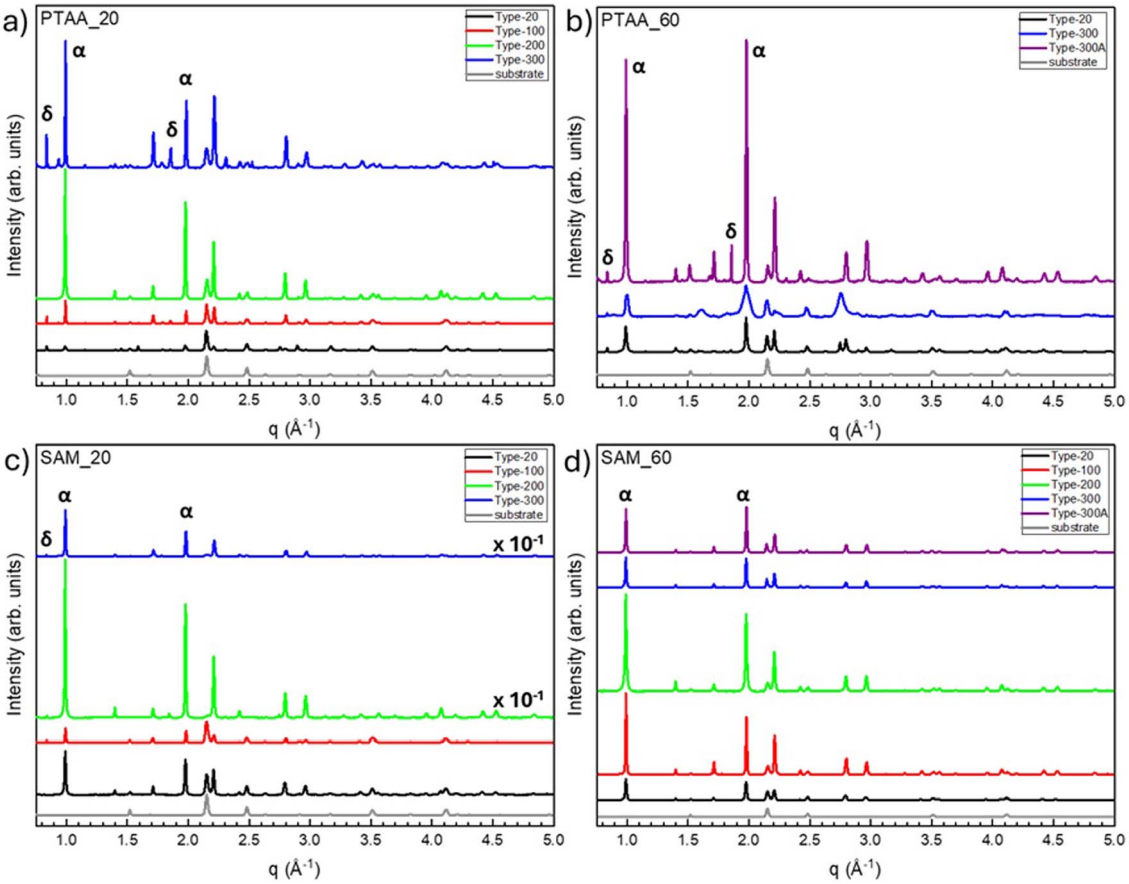

Fig. 3 GIXD plots of $FAPbI_3$ films deposited on PTAA (top plots, a and b)) and the SAM (bottom plots, c and d) at substrate temperatures of 20 °C (left plots, a and c) and 60 °C (right plots, b and d). The perovskite was co-evaporated using different deposition procedures: Type-20 (black curve), Type-100 (red curve), Type-200 (green curve), and Type-300 (blue curve). Type-300A (purple curve) is also included for depositions at 60 °C on both PTAA and the SAM. Substrate spectra are shown in grey as a reference.

temperature. In contrast, the δ-phase appears at this early stage exclusively in PTAA-based samples, indicating distinct interfacial interactions between the growing perovskite film and the underlying HTL. This suggests that the SAM layer is playing a templating role during nucleation, favoring the stabilization of the α-phase over the δ-phase. SAMs have previously been reported to significantly influence $FAPbI_3$ co-evaporation and growth dynamics, mainly due to the presence of phosphonic acids, by promoting α-phase formation and suppressing phase impurities.[39,40,45] Our observations are consistent with these reports, confirming that the presence of SAMs modulates crystallization pathways, ultimately favoring the formation of phase-pure α-$FAPbI_3$ films. In our case, since no post-deposition washing or surface treatment was performed after SAM application, it is likely that the layer is not limited to a compact monolayer. Instead, some unbound *n*PACz molecules may remain on the surface, exposing additional phosphonic acid functional groups. These exposed groups can interact with FAI during deposition, potentially enhancing its incorporation into the growing perovskite film. As reported by Feeney *et al.*, hydrogen bonding between surface iodide ions in the $FAPbI_3$ lattice and phosphonic acid groups of *n*PACz can introduce an energetic barrier that suppresses the transition from the photoactive α-phase to the non-perovskite δ-phase.[39] This interaction may contribute to the improved phase growth and formation observed in our SAM-based samples.

Another key observation is the evolution of α-phase peak intensity, which reaches a maximum at a deposition time of 200 minutes. Beyond this point, the intensity of the two most prominent peaks begins to decline. The initial increase in peak intensity suggests coherent growth of the polycrystalline film, whereas the subsequent decrease likely indicates the onset of disorder in the upper layers (Fig. S8). As deposition progresses, the substrate peak intensity gradually decreases, reflecting reduced X-ray penetration due to increasing perovskite thickness. Simultaneously, the (200) and (210) peak intensities increase, confirming the formation of a thicker and more crystalline perovskite layer. However, at 300 minutes of deposition (Type-300), this trend reverses, suggesting the formation of an amorphous overlayer or increased structural disorder that diminishes the crystalline signal, potentially due to diffuse scattering effects.

To address the issue observed in the Type-300 samples, an intermediate annealing step is introduced in samples named Type-300A to stabilize the perovskite structure and promote further growth of the absorber layer, with the aim of enhancing

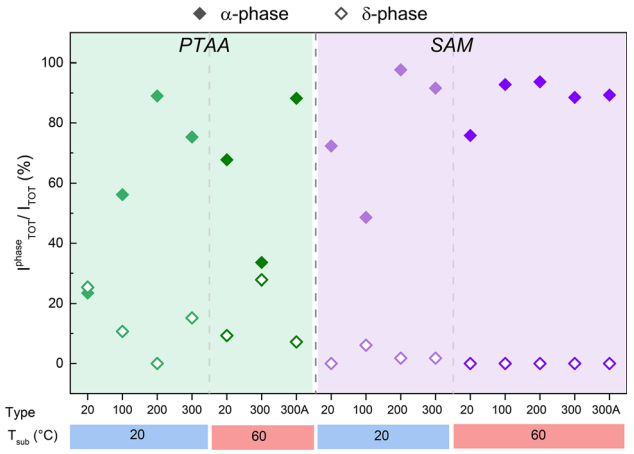

Fig. 4 α- and δ-phase content expressed as the percentage ratio of total peak intensities for each phase over the sum of all peak intensities in the diffraction spectrum, shown for all samples.

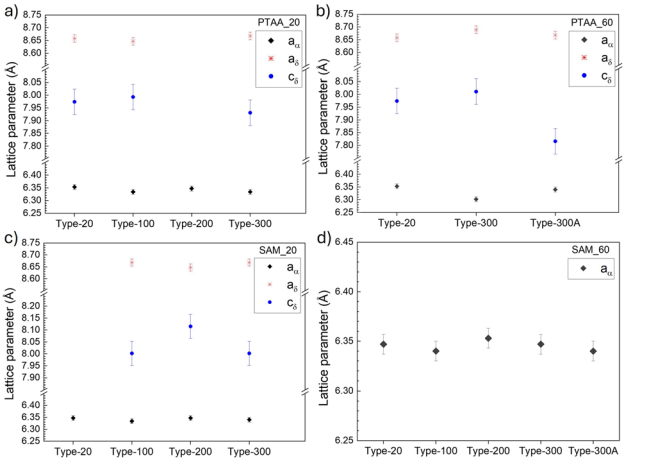

Fig. 5 Lattice parameters estimated from diffraction analysis for $FAPbI_3$ films deposited on PTAA at substrate temperatures of (a) 20 °C and (b) 60 °C and on the SAM at (c) 20 °C. For each sample, the cubic lattice parameter a_α and the hexagonal parameters a_δ and a_δ are reported. In panel (d), corresponding to $FAPbI_3$ grown on the SAM at 60 °C, only the a_α parameter is shown, as no δ-phase reflections were detected.

overall device performance. Structurally, as shown in Fig. 3, the Type-300A samples exhibit higher α-phase peak intensities compared to Type-300, indicating that the additional top-layer deposition is crystalline rather than amorphous and that it integrates with the underlying structure, supporting coherent vertical growth.

A synoptic view of the impact of substrates on the phase purity is shown in Fig. 4. Here, we plot the phase composition of the analyzed samples as estimated by summing the intensities of the diffraction peaks corresponding to each phase normalized to the total intensity of each spectrum. The data show that the intensity associated with the α-phase increases progressively from PTAA to the SAM and also with increasing the substrate temperature from 20 °C to 60 °C. In contrast, the δ-phase exhibits the opposite trend: as the perovskite deposition time increases, the percentage of the δ-phase progressively decreases, except for Type-300. Notably, SAM samples consistently show a lower fraction of δ-phase compared to PTAA, even at short deposition times. Interestingly, in samples deposited on the SAM at 60 °C, the δ-phase component is completely absent, suggesting that higher substrate temperatures promote the stabilization of a pure α-phase on the SAM. Moreover, it is important to note that the α-phase content is increased in the Type-300A samples compared to Type-300, wherever a direct comparison is possible. This supports the conclusion that the intermediate annealing step facilitates crystalline structure recovery in the subsequent layer.

Structural coherence was investigated by observing the relation between q and $\sqrt{(h^2 + k^2 + l^2)}$ for the reflections attributed to the α-phase in PTAA and SAM samples (Fig. S10). The linear relation confirms the expected crystallographic relationship and allows for an exact determination of the lattice parameters.

The calculated lattice parameters for both the cubic (α-phase) and hexagonal (δ-phase) structures are presented in Fig. 5. For the α-phase, no significant differences are observed between PTAA and SAM samples, as the cubic lattice parameter remains essentially constant at an average value of 6.34 ± 0.01 Å across all cases. A slight decrease to 6.33 ± 0.01 Å is found for the PTAA_60 samples, which can be mainly attributed to the smaller number of available data points. Both values, however, are lower than the reported theoretical lattice parameter for α-FAPI, 6.36 Å,[46] indicating the presence of compressive strain with a magnitude of approximately 0.3–0.5%.

Kim *et al.* highlighted that the α-$FAPbI_3$ phase possesses a mechanically soft lattice, rendering it highly sensitive to strain; and even small distortions can significantly affect its structural stability and phase transitions.[47] In polycrystalline perovskite films, residual strain in perovskite films primarily arises from experimental conditions, including the material composition, the choice of the underlayer for film growth, and thermal stress induced during the annealing process or subsequent measurements.[48,49] Importantly, moderate compressive strain has been shown to be beneficial, as it suppresses octahedral tilting, thereby preserving the α-phase structure, limiting ion migration, and elevating the α- to δ-phase transition barrier.[47,50,51]

Several recent studies further suggest that perovskite devices achieve higher efficiencies under compressive strain, which improves band alignment for more effective charge extraction and increases carrier mobility, while simultaneously increasing the formation energy of halide vacancies and suppressing nonradiative recombination. Together, these effects boost open-circuit voltage and fill factor, ultimately contributing to enhanced device performance.[52–55]

Regarding the δ-phase lattice parameters, a more detailed analysis has been performed (Fig. S11), relating the unit cell volume of the δ-phase with the deposition time for SAM and PTAA samples where this phase is detected. Overall, the mean

unit cell volume of the δ-phase remains approximately 519 Å^3, indicating a consistent structure across samples.

However, diffraction data indicate that, although the perovskite absorber deposited on the SAM exhibits improved crystallinity compared to PTAA, the XRD peak intensity is lower (see Fig. 6). The reduced intensity may be attributed to a smaller effective volume of the deposited absorber, which arises from differences in nucleation dynamics on the two studied HTLs. This suggests that the same deposition process may be less effective for one HTL compared to the other. Furthermore, the perovskite film grown on the SAM exhibits a higher density of smaller grains compared to the PTAA-based samples (Fig. S12).

These structural effects are closely related to the interfacial properties of the SAM itself. The molecular packing and orientation of MeO-2PACz, for example, play a critical role in directing the crystallization of the perovskite layer. In particular, despite this favorable influence on crystallinity, such a disordered or excessive SAM can be detrimental to device performance. It may introduce interfacial barriers that hinder efficient charge extraction or lead to variability across large areas. A major limitation is the lack of processing reproducibility, especially over large areas, where achieving uniform SAM coverage is difficult. This directly affects the homogeneity of the device performance.[56–58] Additionally, issues such as micelle formation during deposition can lead to non-uniform film morphology, which in turn hinders efficient interfacial charge transfer.[59,60]

To verify the impact of the HTL and deposition conditions on solar cells obtained with co-evaporated FAPI, we realized PSCs in p–i–n configuration with the following stack: glass/ITO/HTL/FAPI/PCBM/BCP/Cu. Further details are reported in the Experimental section. SAM-based devices exhibit a larger spread of photovoltaic parameters compared to PTAA (Fig. S13), with an overall reduction in PCE mainly driven by a substantial drop in J_{SC}. This drop is likely associated with an excess of organic cations incorporated into the perovskite film, which may arise from altered surface chemistry and growth dynamics, as reported earlier.[39]

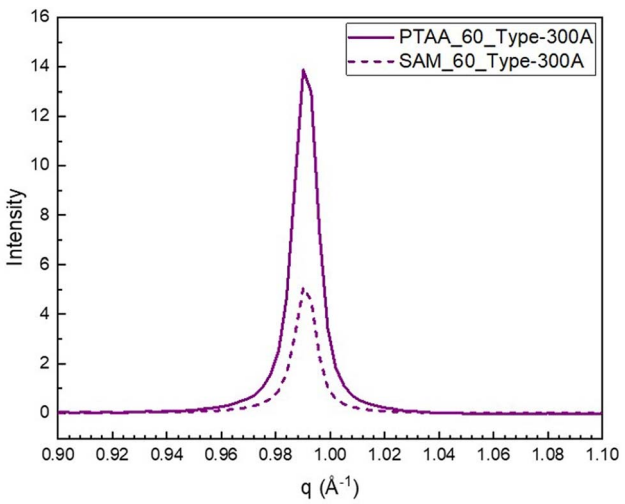

Fig. 6 Comparison of the absolute intensity of the (100) α-phase peak of $FAPbI_3$ perovskite for Type-300A films deposited at 60 °C on PTAA (solid line) and the SAM (dashed line).

We also performed analogous tests on washed SAM substrates, as reported in the SI, observing a similar reduction in J_{SC}, but with improved reproducibility. In this case, the behavior may instead be associated with a relative deficiency of FAI during growth.

In light of these structural and performance-related challenges, PTAA was selected as the HTL for the subsequent device fabrication to ensure improved reproducibility and interface control.

This choice does not imply an intrinsic superiority of PTAA over MeO-2PACz, but rather reflects the better compatibility of the current deposition protocol with PTAA. Additional engineering of the MeO-2PACz/perovskite interface may offer further performance gains, but this aspect is beyond the scope of the present work.

We initially explored $FAPbI_3$ deposition through a continuous 200-minute evaporation process, during which no changes or replacements of the FAI source were made. The resulting devices exhibited good fill factors (FFs), but limited V_{OC} and very low J_{SC}, due to reduced EQE (Fig. S16A and B). These performance losses are attributed to high recombination, consistent with the poor film quality. To mitigate interfacial recombination at surface and grain boundary defects, phenylethylammonium chloride (PEACl) was deposited by thermal evaporation on top of perovskite as a surface passivation layer. Although vapour-phase treatments based on PEA^+ cations were previously explored,[61,62] the use of evaporated PEACl as a passivation layer has not yet been reported, to the best of our knowledge. The introduction of PEACl led to an improvement in V_{OC} (up to ~1.1 V, see Fig. S16 and S17), confirming effective passivation. However, short-circuit current densities were still limited due to the persistent poor quality of the FAPI film.

By combining PEACl passivation with the modified FAPI deposition protocol where two FAI sources were employed sequentially, each for 100 min (Type-200), we achieved a substantial enhancement in photocurrent and EQE, with J_{SC} values approaching 21 mA cm^{-2} (Fig. S16C, D and S17). This optimization led to the best device efficiency of 17.55% (Fig. S16C).

Building on the structural analysis previously presented, Type 300A deposition was selected among Type-300 and Type-300A evaporation protocols with the aim of increasing the FAPI absorber thickness while mitigating the degradation of FAI during prolonged thermal evaporation. In fact, as previously shown, the Type-300A method resulted in films with superior crystallinity compared to Type-300, leading to a more coherent perovskite layer. The perovskite thickness was increased from 280 nm (Type-200) up to 400 nm (Type-300A), without compromising the morphology and the phase (Fig. S18c, d and 7c, d). The (100) diffraction peak of the α-phase appears at 13.91°, slightly shifted from 13.94° in Type-200, indicating strain relaxation with increasing film thickness.[63,64]

Type-300A-based devices showed an enhanced EQE, with integrated J_{SC} approaching 23 mA cm^{-2} achieving a maximum

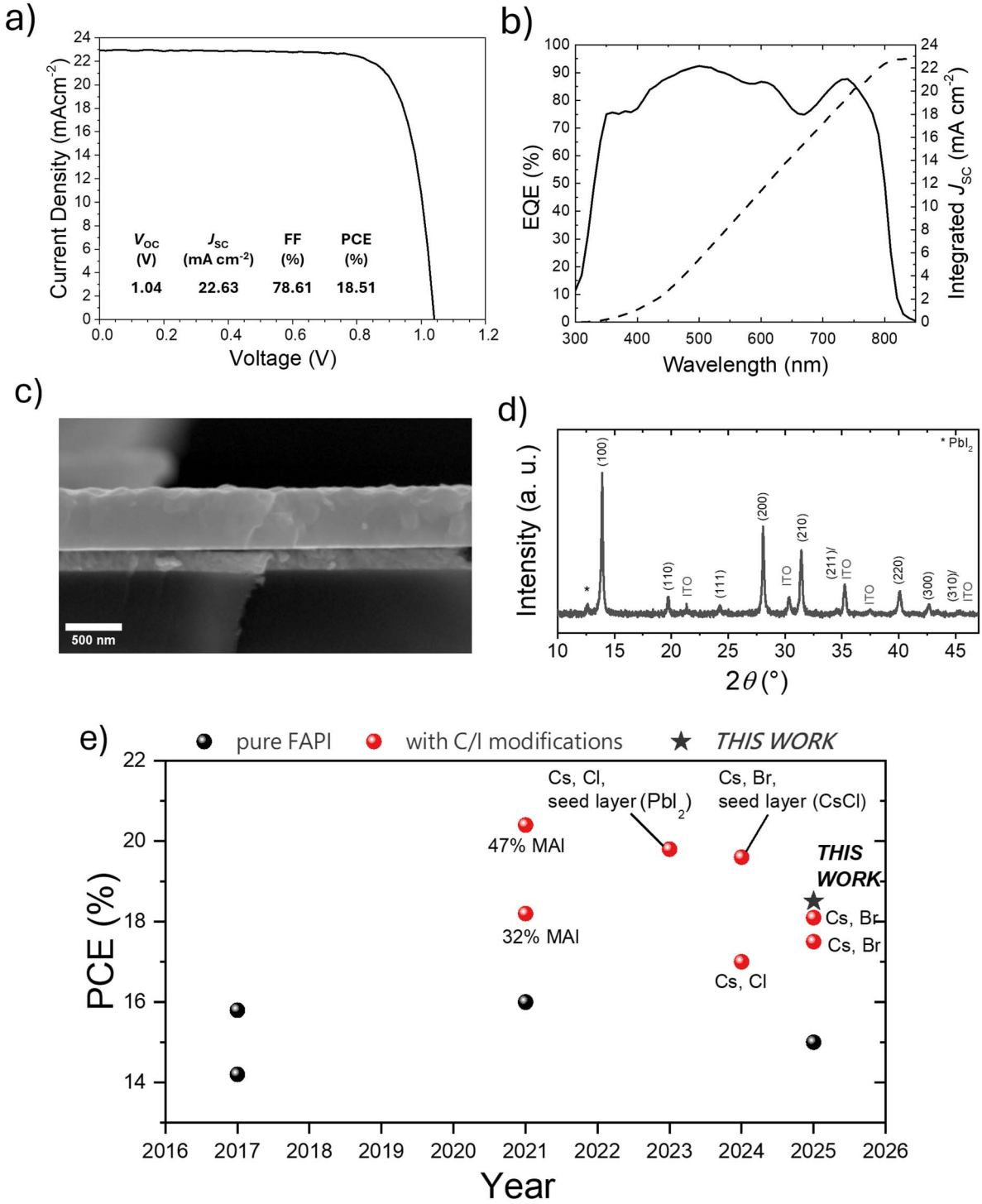

Fig. 7 (a) *J*–*V* and (b) EQE of the Type-300A FAPI-based p–i–n device. The relative electrical parameters are also reported in (a). Statistical distribution of the electrical parameters of the same batch is reported in the SI. (c) SEM cross-section and (d) XRD pattern of glass/ITO/Type-300A FAPI. (e) Power conversion efficiency (PCE) evolution of co-evaporated $FAPbI_3$ solar cells over time. Devices based on pure $FAPbI_3$ (black) and devices with FAPI based on compositional or interfacial (C/I) modifications (red) are compared. The type of C/I modification used is indicated next to each red data point.[38,39,41,66–69] The details are shown in Table S2.

PCE of 18.5% (Fig. 7a and b; statistics in Fig. S19). Notably, this represents one of the highest efficiencies reported for co-evaporated $FAPbI_3$ films without any compositional modification (either cationic or anionic), or seed-layer-assisted interfacial engineering, highlighting the intrinsic quality of the co-evaporated $FAPbI_3$ films (Fig. 7e).

The long-term stability of the devices was evaluated through shelf-life measurements and ISOS-L1 operational stability tests

(Fig. S18). Under shelf-life conditions, the unencapsulated Type-300A-based devices stored in an N_2-filled glovebox exhibit negligible degradation, retaining a stable PCE for 1000 hours (Fig. S20a).

Operational stability under continuous illumination (ISOS-L1), shown in Fig. S20b, reveals an improved durability for the optimized Type-300A architecture, reaching a T_{80} lifetime (defined as the time at which the PCE drops to 80% of its initial value) of 400 hours. In contrast, devices based on the Continuous-200 configuration show a significantly faster performance decay, indicating reduced intrinsic operational stability.

3. Conclusions

In this work, we demonstrate a fully additive-free thermal co-evaporation process for pure $FAPbI_3$ perovskite films, achieving high phase purity and crystallinity through control of deposition dynamics and substrate engineering. By employing multiple FAI sources in a sequential evaporation scheme, we mitigate thermal alterations of the organic precursor and enable the deposition of thick, uniform perovskite layers. Furthermore, the introduction of an intermediate annealing step proves to be critical for enhancing crystallization quality, especially in thicker films, promoting grain growth and improved structural coherence.

We also provide an investigation of the effect of substrate temperature on perovskite film formation. Among the conditions tested, deposition at 60 °C yields the best structural quality, as evidenced by enhanced α-phase formation and suppression of undesired hexagonal phases. Complementary morphological and structural characterization studies, including XRD and GIXD, confirm the improved ordering and orientation of the perovskite films at this temperature. By leveraging a multi-source evaporation scheme, an intermediate annealing step, and optimized substrate temperatures, we establish a framework for improving crystallization dynamics and phase development.

Moreover, the role of the hole transport layer is shown to be pivotal in determining both film quality and device reproducibility, using the same growth protocol. While MeO-2PACz enhances α-phase formation, it suffers from limited processing uniformity and detrimental morphological effects. PTAA, by contrast, enables more reproducible growth and uniform film morphology, ultimately resulting in higher device performance. Using PTAA as the HTL, we achieve a power conversion efficiency of 18.5% in a p–i–n device configuration with pure, thermally evaporated $FAPbI_3$. The devices demonstrated excellent long-term stability (shelf-life) and stable operation under continuous illumination, reaching a T_{80} lifetime of 400 h under ISOS-L1 conditions when encapsulated.

This work offers key insights into the interdependence of process conditions (including precursor evaporation, substrate conditions, and interfacial layers), providing a pathway toward more reliable and scalable fabrication of high-performance vapor-deposited perovskite solar cells.

4. Experimental

4.1 Materials

Indium-tin oxide (ITO)-coated glasses ($R_{SH} = 7\ \Omega\ sq^{-1}$) were purchased from Kintec. Formamidinium iodide (FAI) and phenethylammonium chloride (PEACl) were purchased from GreatCell Solar. Lead(II) iodide (PbI_2) and MeO-2PACz ((2-(3,6-dimethoxy-9*H*-carbazol-9-yl)ethyl)phosphonic acid) were purchased from TCI. Poly[bis(4-phenyl)(2,4,6-trimethylphenyl) amine] (PTAA) SOL2426L (low molecular weight, 5–10 kDa) was purchased from Solaris Chem. Bathocuproine (BCP) and copper beads (Cu beads), ethanol (EtOH) (anhydrous, ≥99.8%), acetone (≥99.5%), chlorobenzene (CB) (99.8%), 1,2-dichlorobenzene (DCB) (99%), toluene (>99.7%), and 2-propanol (IPA) (anhydrous, 99.5%) were purchased from Sigma-Aldrich. Buckminsterfullerene C_{60} (C_{60} purity: 99.5%) and [6,6]-phenyl-C_{60}-butyric acid methyl ester (C_{60}-PCBM purity: 99%) were purchased from Special Carbon Products. Silver (Ag) paste 7713 was purchased from Dupont.

4.2 Device fabrication

The perovskite solar cells were fabricated using an inverted (p–i–n) planar architecture. Glass/ITO substrates were initially patterned using a Yb:KGW raster-scanning laser (Wophotonics, $\lambda = 355$ nm) and subsequently cut into $2.5 \times 2.5\ cm^2$ samples. The patterned substrates were cleaned sequentially in an ultrasonic bath: first in a 2% Hellmanex detergent solution in deionized water, followed by acetone, and finally isopropanol, each for 15 minutes. Any residual solvents were removed using a stream of air. The substrates were then treated with UV-ozone for 15 minutes using a PSD Pro Series Digital UV Ozone System (Novascan) to eliminate remaining organic contaminants.

For PTAA deposition, the substrates were transferred to an air-filled flowbox, where a solution of PTAA (2 mg mL^{-1} in toluene) was spin-coated at 5000 rpm for 20 seconds. In contrast, for SAM deposition, the substrates were transferred to a nitrogen-filled glovebox and coated with MeO-2PACz (0.33 mg mL^{-1} in anhydrous ethanol) *via* spin-coating at 4000 rpm for 30 seconds. All coated samples were subsequently annealed at 100 °C for 10 minutes.

After cooling, the substrates were loaded into a Kenosistec KE 500 K thermal evaporator for the co-deposition of the $FAPbI_3$ perovskite layer. The inner shielding temperature was set to −25 °C, and the substrate temperature was maintained at either 20 °C or 60 °C, with a substrate holder rotation speed of 15 rpm. The amount of precursor loaded into each crucible was measured prior to each deposition process. Specifically, 2.2 g of PbI_2 and 3.0 g of FAI were loaded into their respective crucibles. The crucibles used in our system are conical, with a volume of 10 cm^3. Co-deposition began once the crucible temperatures reached their target temperatures: 345 °C for PbI_2 and 210 °C for FAI, according to the procedures shown in the manuscript (Fig. 1) and as shown in Fig. S23a. In the case of the fresh FAI material, a degassing procedure (preconditioning), during which a pressure increase in the chamber was observed (Fig. S23b), was performed prior to deposition.[32] For Type-200

samples, two different FAI sources were employed sequentially, each for 100 min. After opening the chamber, annealing the samples, and reloading the FAI material, an additional 100 min deposition was carried out to obtain Type-300A FAPI films. The preconditioning step was performed prior to each deposition involving the freshly loaded FAI material. The chamber pressure during deposition was 4–5 $\times$ 10^{-6} mbar. After the process, the samples were annealed in a nitrogen atmosphere at 150 °C for 15 minutes.

To passivate the perovskite layer, PEACl was thermally evaporated at 180 °C for 15 minutes, with no additional annealing.

For the electron transport layer (ETL), the PCBM/BCP stack was deposited by spin-coating. PCBM (27 mg mL^{-1} in a 0.75 : 0.25 CB : DCB mixture) was stirred overnight, then spin-coated at 1350 rpm for 20 seconds and annealed at 100 °C for 3 minutes. Spin-coating of BCP solution (0.5 mg mL^{-1} in IPA) was performed at 2300 rpm for 15 seconds, without further drying.

Finally, 100 nm of copper (Cu) was deposited by thermal evaporation using a shadow mask to define four individual cells per substrate.

The ISOS-L-1 tests were performed with an Arkeo-multichannel platform (Cicci Research company) based on 32 fully independent source meter units (±10 V @ ±250 mA) and an ARKEO light soaker (VIS version) with a low mismatch LED based system (400–750 nm). A standard Perturb & Observe tracking algorithm was selected with a *J–V* scan every 3 hours. The measurements were done under ambient conditions without temperature control, and the cells were encapsulated prior to the test.[65]

4.3 Characterization

J–V measurements of the perovskite solar cells (PSCs) were carried out using a Class-A solar simulator (ABET 2000) equipped with an AM1.5G filter (ABET). The simulator was calibrated to 1 sun illumination using a silicon reference cell (RR-226-O, RERA Solutions). *J–V* characterization in both forward and reverse scan directions was performed using the Arkeo platform (Cicci Research s.r.l.), with a voltage step of 20 mV and a scan rate of 200 mV s^{-1}. An opaque mask defining an active area of 0.09 cm^2 per pixel was applied during the measurements to ensure accurate illumination and measurement. External quantum efficiency (EQE) measurements were conducted using the Arkeo system (Cicci Research s.r.l.), which features a 150 W xenon lamp and a double monochromator covering the 300–1400 nm range. A silicon photodiode was used for incident light calibration before EQE measurement.

X-ray diffraction (XRD) measurements were carried out using a Rigaku SmartLab diffractometer operating in (θ–2θ) Bragg–Brentano geometry. The system was equipped with a Cu Kα radiation source (Kα_1 = 1.54056 Å; Kα_2 = 1.54439 Å) and a D/teX Ultra 250 silicon strip detector. XRD patterns were recorded in a single scan over the 2θ range of 5° to 50°, with a step size of 0.02°, a scan rate of 8° min^{-1}, and a 5 mm entrance slit.

Scanning Electron Microscopy (SEM) measurements were performed by using a FESEM, Tescan Mira 3 LMU FEG. The thickness measurements were acquired with a Dektak Veeco profilometer.

^{1}H-NMR spectra were recorded on a Bruker AVANCE 600 NMR spectrometer (Rheinstetten, Germany) operating at a proton frequency of 600.13 MHz in DMSO-d_6. Chemical shifts (δ) are given in ppm relative to tetramethylsilane (TMS).

Grazing Incidence X-ray Diffraction (GIXD) measurements were performed at the Surfaces Interfaces X-ray Scattering (SixS) beamline at the SOLEIL synchrotron facility (Paris, France). Samples were introduced into an ultra-high vacuum (UHV) chamber and analyzed using an integrated six-circle diffractometer equipped with a 2D hybrid pixel detector (XPAD S70). A 2D hybrid pixel detector (XPAD S70) was used to collect the diffracted intensity, and the BINoculars program was used to process the whole data set. Monochromatic X-rays with a photon energy of 18 keV were used for structural characterization. Preliminary X-ray reflectivity (XRR) measurements were performed to determine the optimal incidence angle. The chosen angle was set to 0.135° above the critical angle of the film and below that of the substrate, ensuring full penetration of the X-ray beam throughout the entire film thickness. Under these conditions, the collected signal originates from the whole bulk of the film while minimizing any contribution from the substrate. The diffracted intensity collected by the detector was processed through the BINoculars program and GIXD scans were acquired at a fixed angle over a scattering vector (q) range of 0.76 $Å^{-1}$ to 5 $Å^{-1}$, with a step size of 0.003 $Å^{-1}$.

Author contributions

F. Z. and E. M.: conceptualization, writing – original draft, software, investigation, formal analysis, data curation, investigation, writing – review & editing. S. P., F. T., E. G., V. R., M. D. G., and F. D. G.: formal analysis, investigation. A. C.: data curation. R. F.: formal analysis, data curation, writing – review & editing. A. D. C.: conceptualization, writing – review & editing, supervision, project administration, funding acquisition.

Conflicts of interest

There are no conflicts to declare.

Data availability

Data for this article, including XRD, *J–V*, EQE, and state-of-the-art references on co-evaporated FAPI, are available at ZENODO at https://doi.org/10.5281/zenodo.17649740.

Supplementary information (SI) is available. See DOI: https://doi.org/10.1039/d5el00193e.

Acknowledgements

E. M. acknowledges the LUMINOSITY project funded by the European Union's Horizon Europe Research and Innovation Programme under grant agreement no. 101147653. F. Z. acknowledges the support of MASE (Ministero dell'Ambiente e della Sicurezza Energetica) in the framework of the Operating

Agreement with ENEA for Research on the Electric System 2025–2027. A. D. C. acknowledges the TANDEM project of Ministero della Transizione Ecologica (Italy), funded on 20/09/2021 (CUP: B83C21001790005). The authors acknowledge Dr Lucia V. Mercaldo for fruitful discussion. The authors wish to thank the SixS beamline staff for the scientific and technical support provided during the experiment at the SOLEIL synchrotron facility.

Notes and references

1 A. U. I. Shah and E. L. Meyer, *Sol. Energy*, 2025, **286**, 113172.
2 W. Xiang and W. Tress, *Adv. Mater.*, 2019, **31**(44), DOI: 10.1002/adma.201902851.
3 W. Shockley and H. J. Queisser, *J. Appl. Phys.*, 1961, **32**, 510–519.
4 Q. Lin, D. J. Kubicki, M. Omrani, F. Alam and M. Abdi-Jalebi, *J. Mater. Chem. C*, 2023, **11**, 2449–2468.
5 H.-S. Kim, A. Hagfeldt and N.-G. Park, *Chem. Commun.*, 2019, **55**, 1192–1200.
6 Y. Ahmed, X. Qi, P. Moazzezi and M. I. Saidaminov, *ACS Energy Lett.*, 2025, **11**(1), 79–89.
7 A. J. Knight and L. M. Herz, *Energy Environ. Sci.*, 2020, **13**, 2024–2046.
8 L. Tian, J. Xue and R. Wang, *Electronics*, 2022, **11**, 700.
9 S. Lee, D. Lee, S. Choi, S. Jung, J. Lee, M. Kim, J. Park and J. Lee, *Sol. RRL*, 2024, **8**(5), DOI: 10.1002/solr.202300958.
10 J. Zhou, Y. Gao, Y. Pan, F. Ren, R. Chen, X. Meng, D. Sun, J. He, Z. Liu and W. Chen, *Sol. RRL*, 2022, **6**(12), DOI: 10.1002/solr.202200772.
11 Y. Liang, F. Li, X. Cui, T. Lv, C. Stampfl, S. P. Ringer, X. Yang, J. Huang and R. Zheng, *Nat. Commun.*, 2024, **15**, 1707.
12 J. Hidalgo, W. Kaiser, Y. An, R. Li, Z. Oh, A.-F. Castro-Méndez, D. K. LaFollette, S. Kim, B. Lai, J. Breternitz, S. Schorr, C. A. R. Perini, E. Mosconi, F. De Angelis and J.-P. Correa-Baena, *J. Am. Chem. Soc.*, 2023, **145**(45), DOI: 10.1021/jacs.3c05657.
13 B. Charles, J. Dillon, O. J. Weber, M. S. Islam and M. T. Weller, *J. Mater. Chem. A*, 2017, **5**, 22495–22499.
14 Z. Zhou, S. Pang, F. Ji, B. Zhang and G. Cui, *Chem. Commun.*, 2016, **52**, 3828–3831.
15 G. E. Eperon, C. E. Beck and H. J. Snaith, *Mater. Horiz.*, 2016, **3**, 63–71.
16 J. Hieulle, X. Wang, C. Stecker, D.-Y. Son, L. Qiu, R. Ohmann, L. K. Ono, A. Mugarza, Y. Yan and Y. Qi, *J. Am. Chem. Soc.*, 2019, **141**, 3515–3523.
17 A. Touré, A. Bouich, B. M. Soucasse and D. Soro, *Opt. Mater.*, 2023, **135**, 113334.
18 H. B. Lee, R. Sahani, V. Devaraj, N. Kumar, B. Tyagi, J. Oh and J. Kang, *Adv. Mater. Interfaces*, 2023, **10**(2), DOI: 10.1002/admi.202201658.
19 W. Cheng, X. He, J. Wang, W. Tian and L. Li, *Adv. Mater.*, 2022, **34**(51), DOI: 10.1002/adma.202208325.
20 Y. Zhang, T. Yang, S.-U. Lee, S. Liu, K. Zhao and N.-G. Park, *ACS Energy Lett.*, 2024, **9**, 159–167.
21 A. Krishna, V. Škorjanc, M. Dankl, J. Hieulle, H. Phirke, A. Singh, E. A. Alharbi, H. Zhang, F. Eickemeyer, S. M. Zakeeruddin, G. N. M. Reddy, A. Redinger, U. Rothlisberger, M. Grätzel and A. Hagfeldt, *ACS Energy Lett.*, 2023, **8**, 3604–3613.
22 Y. Wang, C. Yang, Z. Wang, G. Li, Z. Yang, X. Wen, X. Hu, Y. Jiang, S. Feng, Y. Chen, G. Zhou, J. Liu and J. Gao, *Small*, 2024, **10**(14), DOI: 10.1002/smll.202306954.
23 Z. Huang, Y. Bai, X. Huang, J. Li, Y. Wu, Y. Chen, K. Li, X. Niu, N. Li, G. Liu, Y. Zhang, H. Zai, Q. Chen, T. Lei, L. Wang and H. Zhou, *Nature*, 2023, **623**, 531–537.
24 H. Cao, T. Li, L. Zhao, Y. Qiang, X. Zheng, S. Dai, Y. Chen, Y. Zhu, L. Zhao, R. Cai, Z. Sun, F. Li, Y. Yang, L. Zhang, H.-L. Yip and Z. Yu, *ACS Energy Lett.*, 2025, **10**, 2017–2025.
25 T. Abzieher, D. T. Moore, M. Roß, S. Albrecht, J. Silvia, H. Tan, Q. Jeangros, C. Ballif, M. T. Hoerantner, B.-S. Kim, H. J. Bolink, P. Pistor, J. C. Goldschmidt, Y.-H. Chiang, S. D. Stranks, J. Borchert, M. D. McGehee, M. Morales-Masis, J. B. Patel, A. Bruno and U. W. Paetzold, *Energy Environ. Sci.*, 2024, **17**, 1645–1663.
26 J. Luo, J. Li, L. Grater, R. Guo, A. R. bin Mohd Yusoff, E. Sargent and J. Tang, *Nat. Rev. Mater.*, 2024, **9**, 282–294.
27 J. Li, H. A. Dewi, H. Wang, J. Zhao, N. Tiwari, N. Yantara, T. Malinauskas, V. Getautis, T. J. Savenije, N. Mathews, S. Mhaisalkar and A. Bruno, *Solar RRL*, 2020, **4**(12), 1–8.
28 F. U. Kosasih, E. Erdenebileg, N. Mathews, S. G. Mhaisalkar and A. Bruno, *Joule*, 2022, **6**, 2692–2734.
29 M. Roß, M. B. Stutz and S. Albrecht, *Solar RRL*, 2022, **6**(10), DOI: 10.1002/solr.202200500.
30 B.-S. Kim, M.-H. Choi, M.-S. Choi and J.-J. Kim, *J. Mater. Chem. A*, 2016, **4**, 5663–5668.
31 M. J. Bækbo, O. Hansen, I. Chorkendorff and P. C. K. Vesborg, *RSC Adv.*, 2018, **8**, 29899–29908.
32 M. Kroll, S. D. Öz, R. Ji, Z. Zhang, T. Schramm, T. Antrack, S. Olthof, Y. Vaynzof and K. Leo, *Sustainable Energy Fuels*, 2022, **6**(13), 3230–3239.
33 J. Petry, V. Škorjanc, A. Diercks, T. Feeney, A. Morsa, S. R. Kimmig, J. Baumann, F. Löffler, S. Auschill, J. Damm, D. Baumann, F. Laufer, J. Kurpiers, M. Müller, L. Korte, S. Albrecht, M. Roß, U. W. Paetzold and P. Fassl, *EES Sol.*, 2025, **1**, 404–418.
34 M. Roß, L. Gil-Escrig, A. Al-Ashouri, P. Tockhorn, M. Jošt, B. Rech and S. Albrecht, *ACS Appl. Mater. Interfaces*, 2020, **12**(35), 39261–39272.
35 R. Kottokkaran, H. A. Gaonkar, H. A. Abbas, M. Noack and V. Dalal, *J. Mater. Sci.: Mater. Electron.*, 2019, **30**(6), 5487–5494.
36 K. B. Lohmann, J. B. Patel, M. U. Rothmann, C. Q. Xia, R. D. J. Oliver, L. M. Herz, H. J. Snaith and M. B. Johnston, *ACS Energy Lett.*, 2020, **5**, 710–717.
37 C. Chen, H. Kang, S. Hsiao, P. Yang, K. Chiang and H. Lin, *Adv. Mater.*, 2014, **26**, 6647–6652.
38 L. Gil-Escrig, J. Nespoli, F. D. Elhorst, F. Ventosinos, C. Roldán-Carmona, L. J. A. Koster, T. J. Savenije, M. Sessolo and H. J. Bolink, *EES Sol.*, 2025, **1**, 391–403.
39 T. Feeney, J. Petry, A. Torche, D. Hauschild, B. Hacene, C. Wansorra, A. Diercks, M. Ernst, L. Weinhardt, C. Heske, G. Gryn'ova, U. W. Paetzold and P. Fassl, *Matter*, 2024, **7**, 2066–2090.

40 A. F. Castro-Méndez, F. Jahanbakhshi, D. K. LaFollette, B. J. Lawrie, R. Li, C. A. R. Perini, A. M. Rappe and J. P. Correa-Baena, *J. Am. Chem. Soc.*, 2024, **146**, 18459–18469.
41 M. Roß, S. Severin, M. B. Stutz, P. Wagner, H. Köbler, M. Favin-Lévêque, A. Al-Ashouri, P. Korb, P. Tockhorn, A. Abate, B. Stannowski, B. Rech and S. Albrecht, *Adv. Energy Mater.*, 2021, **11**(35), DOI: 10.1002/aenm.202101460.
42 S. D. Öz and S. Olthof, *ACS Appl. Mater. Interfaces*, 2025, **17**(16), 24535–24546.
43 A. Diercks, J. Petry, T. Feeney, R. Singh, T. Zhao, H. Hu, Y. Li, U. W. Paetzold and P. Fassl, *ACS Energy Lett.*, 2025, 1165–1173.
44 M. V. Khenkin, E. A. Katz, A. Abate, G. Bardizza, J. J. Berry, C. Brabec, F. Brunetti, V. Bulović, Q. Burlingame, A. Di Carlo, R. Cheacharoen, Y. B. Cheng, A. Colsmann, S. Cros, K. Domanski, M. Dusza, C. J. Fell, S. R. Forrest, Y. Galagan, D. Di Girolamo, M. Grätzel, A. Hagfeldt, E. von Hauff, H. Hoppe, J. Kettle, H. Köbler, M. S. Leite, S. (Frank) Liu, Y. L. Loo, J. M. Luther, C. Q. Ma, M. Madsen, M. Manceau, M. Matheron, M. McGehee, R. Meitzner, M. K. Nazeeruddin, A. F. Nogueira, Ç. Odabaşı, A. Osherov, N. G. Park, M. O. Reese, F. De Rossi, M. Saliba, U. S. Schubert, H. J. Snaith, S. D. Stranks, W. Tress, P. A. Troshin, V. Turkovic, S. Veenstra, I. Visoly-Fisher, A. Walsh, T. Watson, H. Xie, R. Yıldırım, S. M. Zakeeruddin, K. Zhu and M. Lira-Cantu, *Nat. Energy*, 2020, **5**, 35–49.
45 S. Kralj and M. Morales-Masis, *Matter*, 2024, **7**, 3238–3240.
46 M. T. Weller, O. J. Weber, J. M. Frost and A. Walsh, *J. Phys. Chem. Lett.*, 2015, **6**, 3209–3212.
47 H. S. Kim and N. G. Park, *Adv. Energy Mater.*, 2025, **15**, 1–10.
48 H.-S. Kim and N.-G. Park, *NPG Asia Mater.*, 2020, **12**, 78.
49 H. Zhang and N. G. Park, *Angew. Chem., Int. Ed.*, 2022, **61**(48), DOI: 10.1002/anie.202212268.
50 Y. Chen, Y. Lei, Y. Li, Y. Yu, J. Cai, M. H. Chiu, R. Rao, Y. Gu, C. Wang, W. Choi, H. Hu, C. Wang, Y. Li, J. Song, J. Zhang, B. Qi, M. Lin, Z. Zhang, A. E. Islam, B. Maruyama, S. Dayeh, L. J. Li, K. Yang, Y. H. Lo and S. Xu, *Nature*, 2020, **577**, 209–215.
51 J. Dai, T. Li, X. Li, C. Xu, M. Zhao, H. Cai and X. Wu, *Phys. Chem. Chem. Phys.*, 2025, **27**, 16783–16793.
52 Y. Zhou, Z. Guo, S. M. H. Qaid, Z. Xu, Y. Zhou and Z. Zang, *Sol. RRL*, 2023, **7**, 1–26.
53 G. Liu, M. Ghasemi, Q. Wei, G. Zhang, J. Luo, D. Su, B. Jia, Y. Yang and X. Wen, *ACS Appl. Mater. Interfaces*, 2025, **17**, 36706–36716.
54 J. Cao, R. Yuan, B. Cai, C. Wu and X. Zheng, *Adv. Energy Sustainability Res.*, 2023, **4**(4), DOI: 10.1002/aesr.202200143.
55 X. Jiang, X. Wang, X. Wu, S. Zhang, B. Liu, D. Zhang, B. Li, P. Xiao, F. Xu, H. Lu, T. Chen, A. K. Y. Jen, S. Yang and Z. Zhu, *Adv. Energy Mater.*, 2023, **13**, 1–8.
56 T. Liu, C. Luo, R. He, Z. Zhang, X. Lin, Y. Chen and T. Wu, *Adv. Mater.*, 2025, **37**(48), DOI: 10.1002/adma.202502032.
57 C. Fei, A. Kuvayskaya, X. Shi, M. Wang, Z. Shi, H. Jiao, T. J. Silverman, M. Owen-Bellini, Y. Dong, Y. Xian, R. Scheidt, X. Wang, G. Yang, H. Gu, N. Li, C. J. Dolan, Z. J. D. Deng, D. N. Cakan, D. P. Fenning, Y. Yan, M. C. Beard, L. T. Schelhas, A. Sellinger and J. Huang, *Science*, 2024, **384**, 1126–1134.
58 L. Li, Y. Wang, X. Wang, R. Lin, X. Luo, Z. Liu, K. Zhou, S. Xiong, Q. Bao, G. Chen, Y. Tian, Y. Deng, K. Xiao, J. Wu, M. I. Saidaminov, H. Lin, C.-Q. Ma, Z. Zhao, Y. Wu, L. Zhang and H. Tan, *Nat. Energy*, 2022, **7**, 708–717.
59 Y. Yuan, H. Li, H. Luo, Y. Zhang, X. Li, T. Jiang, Y. Yang, L. Liu, B. Fan and X. Hao, *Energies*, 2025, **18**(10), 2577.
60 M. Liu, L. Bi, W. Jiang, Z. Zeng, S. Tsang, F. R. Lin and A. K.-Y. Jen, *Adv. Mater.*, 2023, **35**(46), DOI: 10.1002/adma.202304415.
61 C. A. R. Perini, A.-F. Castro-Mendez, T. Kodalle, M. Ravello, J. Hidalgo, M. Gomez-Dominguez, R. Li, M. Taddei, R. Giridharagopal, J. Pothoof, C. M. Sutter-Fella, D. S. Ginger and J.-P. Correa-Baena, *ACS Energy Lett.*, 2023, **8**, 1408–1415.
62 M.-G. La-Placa, L. Gil-Escrig, D. Guo, F. Palazon, T. J. Savenije, M. Sessolo and H. J. Bolink, *ACS Energy Lett.*, 2019, **4**, 2893–2901.
63 P. Shi, J. Xu, I. Yavuz, T. Huang, S. Tan, K. Zhao, X. Zhang, Y. Tian, S. Wang, W. Fan, Y. Li, D. Jin, X. Yu, C. Wang, X. Gao, Z. Chen, E. Shi, X. Chen, D. Yang, J. Xue, Y. Yang and R. Wang, *Nat. Commun.*, 2024, **15**, 2579.
64 M. Rai, L. H. Wong and L. Etgar, *J. Phys. Chem. Lett.*, 2020, **11**, 8189–8194.
65 P. Mariani, M. Á. Molina-García, J. Barichello, M. I. Zappia, E. Magliano, L. A. Castriotta, L. Gabatel, S. B. Thorat, A. E. Del Rio Castillo, F. Drago, E. Leonardi, S. Pescetelli, L. Vesce, F. Di Giacomo, F. Matteocci, A. Agresti, N. De Giorgi, S. Bellani, A. Di Carlo and F. Bonaccorso, *Nat. Commun.*, 2024, **15**, 4552.
66 J. Borchert, R. L. Milot, J. B. Patel, C. L. Davies, A. D. Wright, L. Martínez Maestro, H. J. Snaith, L. M. Herz and M. B. Johnston, *ACS Energy Lett.*, 2017, **2**, 2799–2804.
67 T. C.-J. Yang, T. Kang, M. Fitzsimmons, G. Vega, Y. Lu, L. Rosado, A. Jiménez-Solano, L. Pan, S. J. Zelewski, J. Ferrer Orri, Y. Chiang, D. Guo, Z. Y. Ooi, Y. Han, W. Xu, B. Roose, C. Ducati, S. Carretero Palacios, M. Anaya and S. D. Stranks, *EES Sol.*, 2025, **1**, 41–55.
68 S. Yan, J. B. Patel, J. E. Lee, K. A. Elmestekawy, S. R. Ratnasingham, Q. Yuan, L. M. Herz, N. K. Noel and M. B. Johnston, *ACS Energy Lett.*, 2023, **8**, 4008–4015.
69 V. Škorjanc, A. Miaskiewicz, M. Roß, S. Maniyarasu, S. Severin, M. R. Leyden, P. Holzhey, F. Ruske, L. Korte and S. Albrecht, *ACS Energy Lett.*, 2024, **9**, 5639–5646.

